39th AIAA Fluid Dynamics Conference
22 - 25 June 2009, San Antonio, Texas

AIAA 2009-4212

Computation of the Flow of a Dual-Stream Jet with Fan-Flow Deflectors for Noise Reduction

Juntao Xiong *, Feng Liu † and Dimitri Papamoschou ‡

University of California Irvine, Irvine, CA, 92697, USA

This paper studies the impact of installing noise-suppressing deflector vanes in the bypass flow on the aerodynamic performance of the dual-stream supersonic nozzle of a turbofan engine by using a three-dimensional Reynolds-averaged Navier-Stokes computer program. A series of nozzle configurations using a single pair or double pairs of vanes with NACA0012, NACA4412, and NACA7514 airfoil profiles are investigated. The effects of the azimuthal mounting position of the deflector vanes, angle of attack, and shape of the airfoils are studied. The flow field around the vanes, overall flow turning angle, reduction of turbulent kinetic energy, thrust loss, and blockage caused by the deflector vanes are examined. Recommendations regarding the choice of airfoil and mounting configurations are made for best noise suppressing effectiveness with minimum loss of thrust and mass flow.

Nomenclature

NPR	=	nozzle pressure ratio
W	=	conservative variable vector
F_c	=	inviscid convective flux
F_d	=	inviscid diffusive flux
Ω	=	control volume
ρ	=	density
x, y, z	=	Cartesian coordinates
u, v, w	=	velocity components
E	=	total internal energy
k	=	turbulent kinetic energy
ω	=	specific dissipation rate
p	=	static pressure
q	=	dynamic pressure
α	=	angle of attack, closure coefficient
β, β^*	=	closure coefficients
γ	=	specific heat ratio
ϵ	=	plume deflection angle
μ_L	=	molecular viscosity
μ_T	=	turbulent viscosity
τ	=	stress tensor
σ^*	=	closure coefficient
M	=	Mach number
c	=	vane chord length
D_f	=	nozzle fan diameter
r	=	radial direction
$\mathcal{L}$	=	lift force

*Post-doctoral Researcher, Department of Mechanical Aerospace Engineering, Member AIAA
†Professor, Department of Mechanical and Aerospace Engineering, Associate Fellow AIAA
‡Professor, Department of Mechanical and Aerospace Engineering, Fellow AIAA

C_p	=	pressure coefficient
$\mathcal{T}$	=	thrust
ϵ	=	plume deflection angle

Subscript

a	=	ambient
e	=	exit
LE	=	vane leading edge
MID	=	vane mid chord
TE	=	vane trailing edge
p	=	primary exhaust
s	=	secondary exhaust

I. Introduction

The idea of tilting the bypass stream with fan flow deflectors of a turbofan engine to reduce jet noise was proposed by Papamoschou.[1,2] Figure 1 depicts the general concept. Vanes are installed in the secondary flow stream. These vanes deflect the secondary flow downward. The overarching principle of the concept is the reduction of the convective Mach number of the turbulent eddies generated by the high speed hot core flow. Mean flow surveys show that the misaligment of the two flows causes a thick, low-speed secondary core on the underside of the high-speed primary flow, especially in the region near the end of the primary potential core, which contains the strongest noise sources. The secondary core reduces the convective Mach number of the primary eddies, thus hindering their ability to generate sound that travels to the downward far field. Past subscale experiments have demonstrated significant reductions in perceived noise level.[3,4]

As with any noise reduction scheme, it is important to assess the aerodynamic efficiency. Meaningful reduction of noise must take into account the aerodynamic performance. Because of the difficulties and cost involved in experimentally evaluating the effect of fan deflectors on the aerodynamic performances of the nozzle, computational studies are used. Papamoschou and Liu[5] evaluated the aerodynamic performance of a pair of vane deflectors installed in the bypass duct of a dual-stream nozzle. Details of the flow field around the vanes in the accelerating bypass stream are computed by using a RANS method. The problem was simplified by limiting the computational domain to the exit of the bypass duct, this means the effect of the ambient air and the interaction with the primary jet were neglected. The present study extends the computational domain to include the shear layer between the primary jet and secondary jet and the shear layer between the ambient air and the secondary jet. The purpose of this study is to establish an accurate computational method for simulating the dual-stream nozzle flows including the jets, and use it to gain insight into the flow filed of the internal vanes and assess their impact on the aerodynamic performances of the nozzle.

A three-dimensional Reynolds-averaged Navier-Stokes code with the SST k-ω turbulence model is used for the present study. The code is first validated against experimental data on the mean velocity profiles of the jet. It is then used to simulate a series of vane configurations at engine cycle condition to investigate the impact on nozzle aerodynamic performance. Three different airfoils and a number of mounting configurations are studied. The computational analysis include the flow field features of internal airfoil vanes, the effect on thrust and mass flow rate of the deflector vanes, and the effectiveness of vanes in deflecting the fan flow downward.

II. Computational Approach

II.A. Numerical Code

The computational fluid dynamics code used here is known as PARCAE and solves the unsteady three-dimensional Reynolds-averaged Navier-Stokes (RANS) equations on structured multiblock grids using a cell-centered finite-volume method with artificial dissipation as proposed by Jameson et al.[6] Information exchange for flow computation on multiblock grids using multiple CPUs is implemented through the MPI (Message Passing Interface) protocol. The RANS equations are solved using the eddy viscosity type turbulence models. The code contains the Baldwin-Lomax algebraic model[7] , Spalart-Allmaras one-equation model,[8] k-ω two-equation model,[9] and Menter SST k-ω model.[10] In this study, only the steady-state solution is obtained because we are interested in the time-averaged features of the flow. All computations presented in this work are performed using the SST model. The SST turbulence model combines the advantages of the k-ω and k-ϵ turbulence models for both wall boundary layer and free-stream flows. The main elements of the code are summarized below.

The governing equations for the unsteady compressible turbulent flow with a SST turbulence model are expressed as follows:

$$\frac{\partial}{\partial t}\int_{\Omega} \mathbf{W}\, d\Omega + \oint_{\partial\Omega} (\mathbf{F}_c - \mathbf{F}_d)\, dS = \int_{\Omega} \mathbf{S}\, d\Omega \tag{1}$$

The vector $\mathbf{W}$ contains the conservative variables

$$\mathbf{W} = \left\{ \; \rho, \rho u, \rho v, \rho w, \rho E, \rho k, \rho\omega \; \right\}^{\mathrm{T}} \tag{2}$$

The fluxes consist of the inviscid convective fluxes $\mathbf{F}_c$ and the diffusive fluxes $\mathbf{F}_d$. For the convective fluxes we include the pressure term

$$\mathbf{F}_c = \left\{ \begin{array}{ccc} \rho u & \rho v & \rho w \\ \rho uu + p & \rho uv & \rho uw \\ \rho vu & \rho vv + p & \rho vw \\ \rho wu & \rho wv & \rho ww + p \\ \rho Eu + pu & \rho Ev + pv & \rho Ew + pw \\ \rho ku & \rho kv & \rho kw \\ \rho\omega u & \rho\omega v & \rho\omega w \end{array} \right\} \tag{3}$$

For the diffusive fluxes we have

$$\mathbf{F}_d = \left\{ \begin{array}{ccc} 0 & 0 & 0 \\ \tau_{xx} & \tau_{xy} & \tau_{xz} \\ \tau_{yx} & \tau_{yy} & \tau_{yz} \\ \tau_{zx} & \tau_{zy} & \tau_{zz} \\ \theta_x & \theta_y & \theta_z \\ \mu_k^* \frac{\partial k}{\partial x} & \mu_k^* \frac{\partial k}{\partial y} & \mu_k^* \frac{\partial k}{\partial z} \\ \mu_\omega^* \frac{\partial \omega}{\partial x} & \mu_\omega^* \frac{\partial \omega}{\partial y} & \mu_\omega^* \frac{\partial \omega}{\partial z} \end{array} \right\} \tag{4}$$

where

$$\begin{aligned} \mu_k^* &= \mu_L + \sigma_k \mu_T \\ \mu_\omega^* &= \mu_L + \sigma_\omega \mu_T \\ \mu_T &= \frac{\rho a_1 k}{max(a_1\omega; \omega F_2)} \end{aligned}$$

and

$$\begin{aligned} \theta_x &= u\tau_{xx} + v\tau_{xy} + w\tau_{xz} + \mu^* \frac{\partial k}{\partial x} \\ \theta_y &= u\tau_{xy} + v\tau_{yy} + w\tau_{zy} + \mu^* \frac{\partial k}{\partial y} \\ \theta_z &= u\tau_{xz} + v\tau_{yz} + w\tau_{zz} + \mu^* \frac{\partial k}{\partial z} \\ \mu^* &= \mu_L + \sigma^* \mu_T \end{aligned}$$

with τ being the stress tensor. The source term is

$$\mathbf{S} = \left\{ \begin{array}{c} 0 \\ 0 \\ 0 \\ 0 \\ 0 \\ \tau_{ij}\frac{\partial u_i}{\partial x_j} - \beta^* \rho \omega k \\ \frac{\gamma}{\nu_t}\tau_{ij}\frac{\partial u_i}{\partial x_j} - \beta\rho\omega^2 + 2\rho(1-F_1)\frac{1}{\omega}\frac{\partial k}{\partial x_j}\frac{\partial \omega}{\partial x_j} \end{array} \right\} \tag{5}$$

In the above equations, F_1 and F_2 are blending functions. The parameters σ_k, σ_ω, β, β^*, and γ are closure coefficients for the turbulence model. The equations are discretized in space by a structured hexahedral grid using a cell-centered finite-volume method. Since within the code each block is considered as a single entity, only flow and turbulence quantities at the block boundaries need to be exchanged. The governing equations are solved explicitly in a coupled manner through a five stage Runge-Kutta scheme towards the steady state with local-time stepping, residual smoothing, and multigrid for convergence acceleration. A low-speed preconditioner[11] is employed to simulate low ambient Mach number of the nozzle and jet plume flows. Further details of the numerical method can be found in Ref. 12.

II.B. Computational Model and Grid

The dual-stream BPR=2.7 (B27) nozzle model is used for this computational study. The fan exit diameter is $D_f = 28.1$ mm, and the fan exit height is 1.8 mm. Details of the thermodynamic cycle of the B27 nozzle can be found in Ref. 3. The B27 nozzle radial coordinates is shown in Fig. 2. Jet plume deflection is achieved by the use of internal airfoil-shaped vanes. Configurations consisting of single and double pairs of vanes with NACA0012, NACA4412, and NACA7514 airfoil profiles are studied. The vanes are placed at various azimuth angles and angles of attack. For all cases simulated the vane chord length is 3 mm and the vane trailing edge is situated 2 mm upsream of the nozzle exit. Table 1 lists the details of the configurations. Figure 3 shows the 2-vane and 4-vane configurations.

Multiblock grids are generated for each vane configuration. Because all the vane configurations are symmetric to the meridional plane, only one half (180°) of the nozzle was modeled to save computation cost. In order to simulate the jet flow, the grids extended about $3.8D_f$ radially outward from the nozzle centerline and over $20D_f$ downstream of the nozzle. A C-grid surrounds each vane in the region near the exit plane to capture the features of boundary layer and wake flows accurately. The outer-region grids for all cases are kept the same to simplify grid generation work. A patch-connection interpolation technique is used to transfer flow variables information between non-matching connection surfaces. Figure 4 shows the complete nozzle grid and the grid around the vane of a typical 4-vane configuration.

II.C. Flow and Boundary Conditions

The experimental tests were performed with static free-stream conditions. The engine operating conditions of the B27 nozzle are shown in Table 2. The hot condition matches the condition determined by the engine cycle analysis and is used in the acoustic tests while the cold condition is that used in the mean velocity tests. The cold condition is used to validate the computational simulations while the hot condition is used for the aerodynamic performance investigation. For the cold case the total temperature of both streams is set to the ambient value. For numerical stability, computations are performed with a free-stream velocity of 17 m/s (M=0.05). The flow conditions imposed at the various boundaries are the same for both cases. For the fan and core duct flows uniform total pressure, total temperature, and zero flow angle are specified at the inlet surface corresponding to a perfectly expanded exit Mach number. For the ambient region surrounding the nozzle flow, a characteristic boundary condition is defined, and the downstream static pressure is set to the ambient pressure. The adiabatic no-slip boundary condition is specified on all nozzle and vane solid walls. The jet Reynolds number for the hot and cold conditions are 0.92×10^6 and 0.47×10^6, respectively, based on the exit diameter of the fan nozzle .

II.D. Aerodynamic Parameters

In order to obtain the engine aerodynamic performace, a control volume that includes the entire engine is selected. Considering the nozzle discharge at static condition. The nozzle thrust is obtained by integration of the axial momentum and pressure on the exit surface of the control volume and subtracting the contribution from the free-stream.

$$\mathcal{T} = \int_A (\rho u^2 + p - p_a) dA \tag{6}$$

The mass flow rate is obtained by integration of mass flux on the fan and core nozzle exit surfaces.

$$\dot{m} = \int_{A_{p+s}} \rho u dA \tag{7}$$

The overall lift of the nozzle is obtained by integration of the transverse momentum flux on the control volume exit surface and subtracting the contribution from the free-stream

$$\mathcal{L} = \int_A \rho v u dA \tag{8}$$

and, assuming small angles, the overall deflection of the plume is

$$\epsilon = \frac{\mathcal{L}}{\mathcal{T}} \tag{9}$$

The thrust loss and mass flow rate loss are defined as

$$\Delta\mathcal{T} = \mathcal{T} - \mathcal{T}_{\text{clean}} \tag{10}$$

$$\Delta\dot{m} = \dot{m} - \dot{m}_{\text{clean}} \tag{11}$$

where the subscript "clean" refers to the clean nozzle without vanes. The airfoil flows studied here are fairly unique in that they are subjected to an *externally imposed favorable pressure gradient.* In other words, because of the convergence of the nozzle, the "freestream" velocity accelerates in the axial direction. Definition of the aerodynamic coefficient becomes problematic as there is no fixed reference condition. Here we make the somewhat arbitrary selection of using as reference the area-averaged conditions in the plane of the vane leading edge (LE) in the absence of the vane. The pressure coefficient is defined as

$$C_p = \frac{p - p_{\text{LE}}}{q_{\text{LE}}}, \tag{12}$$

III. Results and Discussion

The computations are first validated with experimental measurements of the mean velocity field at the cold condition. Then the code is extended to the hot condition to investigate the impact on nozzle aerodynamic performance of the fan flow deflector.

III.A. Validation Against Mean Flow Measurement

The computational code is validated by comparing the computed axial velocity of the jet to experimental measurements. The results of the baseline nozzle and the 4V-D nozzle at the cold condition are shown in Figs. 5(a) and 5(b), respectively. The comparison of velocity contours at the symmetry plane indicates that the lengths of the potential core are very similar. The growth rate of the computational and experimental jets are very close. The velocity contours in cross sectional planes and the velocity profile along the vertical diameter are also shown in the figure at three different axial locations. The computed velocity contours show perfectly circular shapes while the experimental measurement show almost perfect circles for the baseline case where there are no deflector vanes in the nozzle. The velocity profiles match the experimental ones well except at the center line close to the nozzle exit where the computational result shows a deeper deficit behind the nozzle center cone. This difference, however, becomes smaller as the flow moves downstream. The computational result also shows a slightly larger free-stream velocity because of the non-zero free-stream velocity condition.

In the 4V-D nozzle case shown in Fig. 5(b), both the computed and experiment velocity contours at the three cross sections show clear oval shapes with notable thickening of the secondary jet layer beneath the primary jet, which accounts for the reduction of noise emitting downward. Again the computed velocity profiles match well those of the experiment.

More detail of these and other validation data are presented in Ref. 13. The close agreements between the computed results with experiments lend confidence for us to apply the computational code to evaluate the influence of the deflector vanes on the aerodynamic performance of the different nozzle configurations.

III.B. Flow Field Around the Deflector Vanes

The flow field around the deflector vanes is exammed in order to gain insight into the effectiveness for flow turning and the corresponding aerodynamic performance of the different choices of airfoils, angle of attack, and mounting positions of the airfoils. Only the 4-vane configurations list in Table 1 are studied. The 2-vane configuration, Fig. 3(a), is found to yield very small turning. Figures 6-11 show the computed Mach contours at the mid-span section of the deflector vanes in the bypass nozzle for the 6 4-vane configurations. Figure 12 shows the corresponding pressure distributions on the airfoil. The C_p^* line marks the critical pressure coefficient where the flow becomes sonic.

The first 3 configurations all use two pairs of the same NACA0012 airfoil mounted at the $\phi_1 = 50°$ and $\phi_2 = 120°$ azimuth angles as shown in Fig. 3(b). The airfoils are set, however, at 3 different angles of attack relative to the axial flow 0°, 7.5° and 10°, for the 4V-A, 4V-B, and 4V-C configurations, respectively. Both the Mach contours shown in Figs. 6-8 and the pressure distributions shown in Fig. 12(a)-12(c) indicate an accelerating mainstream around the airfoil. This is the consequence of the imposed favorable pressure ratio across the nozzle. The overall favorable pressure gradient of the nozzle flow gives rise to the thin boundary layers over the airfoil and the limited wakes, which result in small flow loss and mass flow blockage to our advantage. However, as the angle of attack increases, the Mach contours and the surface pressure distribution reveal a sharp suction peak at the leading edge of the airfoil followed by a strong pressure diffusion behind the peak, which thickens the boundary layer and therefore results in increased drag. In addition this suction peak may cause a supersonic pocket with a possible shock wave at higher angles of attack. Both the shock wave and possible shock induced separation would cause flow loss and blockage, and therefore should be avoided. At 10° angle of attack, the 4V-C case shows a small supersonic bubble near the leading-edge. This peaky behavior of the flow could be avoid by a redesign of the airfoil for optimal loading in the accelerating nozzle stream.

In order to investigate the effect of the azimuthal positions of the airfoils, Figs. 9 and 12(d) examine the flow field of the 4V-D configuration, where the same symmetric NACA0012 airfoils are mounted at $\phi_1 =$ 90° and $\phi_2 = 150°$ azimuth angle as shown in Fig. 3(c). The airfoils are set at an angle of attack of 7.5°. Compare to the similar 4V-B case, there appears to be small differences between the two flows. However, discussions in the next subsection will show differences in their overall aerodynamic performances.

Figures 10 and 12(e) examine the effect of using a cambered airfoil, the NACA7514, airfoil as compared to the symmetric NACA0012 airfoil. The azimuthal mounting positions are the same as those for the first 3 4-V cases. Because the airfoil is cambered, a smaller angle of attack (4°) is set for this configuration. Despite the small angle of attack, both the Mach contours and the surface pressure distribution show a large supersonic pocket with a strong terminating shock wave on the back of the airfoil. The camber overloads the rear portion of the airfoil, resulting in a large suction area in the accelerating main stream.

Figures 11 and 12(f) examines the 4V-F configuration, where the NACA7514 airfoil is replaced by the less cambered and thinner airfoil NACA4412. The mounting azimuth angles are the same as those for 4V-D configuration. The less symmetric azimuth angle positions result in a more obvious asymmetric in the pressure distribution over the 2 airfoils. The decreased camber and thickness have reduced the suction peaks compared to those on the NACA7514 airfoil. However, the general trend of the flow with an overloaded rear pressure distribution is the same. These results seem to indicate that a conventional cambered design of the airfoil may not be desirable in such an accelerating flow environment.

III.C. Effectiveness of the Vanes and Their Impact on Aerodynamic Performance

In this subsection we examine the effectiveness of vanes for flow turning and their impact on the overall engine thrust and mass flow rate. Equations (6)-(11) are used to calculate the thrust loss, mass flow loss and deflection angle. Results for all the configurations are listed in Table 3.

For the 2V case, the deflection angle is only 0.584° that is insufficient for significant noise reduction despite the relatively large 7.5° angle of attack. The mass flow loss and thrust loss are relatively low, 0.046% and 0.076% respectively. However, further increase of the angle of attack to obtain sufficient flow turning may cause a severe supersonic suction peak at the leading edge of the airfoil and therefore results in large flow losses. For the 4V cases with the NACA0012 airfoil, the deflection angle increases with increase of the angle of attack. At zero angle of attack, the deflection angle is zero, and the mass flow loss and thrust loss are 0.008% and 0.047%, respectively. At conditions where noise suppression is not important, such as cruise, the angle of attack of the vanes can be set to 0° since this configuration has the least impact on nozzle performance. At 7.5° angle of attack, the deflection angle is 0.938°, the corresponding mass flow loss and thrust loss are 0.152% and 0.237%, respectively. Because the flow is free from shock waves and separation the penalties on the nozzle aerodynamics are relatively small and acceptable for realistic applications. When the angle of attack increases from 7.5° to 10°, the mass flow loss and thrust loss increase by about 70% while the deflection angle is only increased by 40%. For the 4V-D configuration where the NACA0012 vanes are placed at the azimuth angles of 90° and 150° with 7.5° angle of attack, the deflection angle is reduced by 13.2% compared to the 4V-B configuration where the airfoil are also at 7.5°. The thrust loss and mass flow loss, however, are reduced by about 50%. This may indicate that the 90° and 150° azimuth locations might be better than those at 50° and 120°.

The cambered airfoil are very effective in deflecting the flow at the same or smaller angles of attack compared to the symmetric airfoil. The deflection angles are 1.331° for the NACA7514 configuration and 1.168° for the NACA4412 configuration. However, as discussed in the previous subsection, the cambered airfoils cause severe overloading over the rear portion of the airfoil. That result in shock waves and boundary layer thickening and possible separation. The thrust loss and mass flow blockage are more than proportionally increased, especially for the NACA7514 case, which has 0.72% thrust loss and 0.56% mass loss. The NACA4412 case has a little better numbers than the NACA7514 case because of the reduced camber and thickness. Nevertheless, its losses are still significant.

Regardless of the choice of airfoils, there is a general correlation between the losses of thrust and mass flow and the deflection angle as shown in Fig. 13. The losses are low when the deflection angle is small but they increase drastically when the deflection angle increases over a certain critical value, which is about 1.0° based on the limited configurations studied here .

Figure 14 shows the Turbulent kinetic energy (TKE) contours in the x-y plane for the baseline nozzle and 4 4-V nozzles. The turbulence kinetic energy k is normalized in the form $k^* = \frac{k}{U_p^2}$. The plot of TKE contours clearly shows that deflecting the secondary jet downward by the vanes in the bypass duct has the effect of decreasing the TKE on the lower side of the jet with an increase of TKE on the upper side. The peak values of k^* on the lower and upper sides of the jet are list in Table 4 for all the different configurations. The lower side peak value of TKE reduction versus deflection angle is shown in Fig. 15.

TKE in the flow field has been found to correlate with noise level.[13] Figure 16 shows a correlation between reduction of the peak overall sound pressure level (OASPL) and TKE at $x/D_f = 5.6$. The correlation shows a hyperbolic tangent-like trend that suggests a rapid increase in noise reduction for small reductions of TKE. However, the noise reduction levels off as the reduction of TKE increases. A balanced choice of deflection angle for maximum noise reduction with minimum acceptable thrust loss might be made by looking at Fig. 13, 14, and 16 at the same time. Based on the limited configurations studied without optimizing the airfoils, a 3.6 dB (OASPL) reduction corresponds to a deflection angle of 0.9°, which is narrowly below the drastic thrust increase threshold. From among the configurations shown in Table 3, it appears that the 4V-B or 4V-D configurations offer the best choices. As discussed in the previous subsection where the detailed flow on the airfoils are examined, further research should be conducted in search for an optimized airfoil shape suitable for effective flow turning in an accelerating main stream with minimum thrust loss.

IV. Conclusions

A computational study is conducted of the flow in the dual-stream nozzle of a turbofan engine with several fan flow deflector configurations. The aim of the investigation is to analyze the flow field of the internal vanes and quantify their impact on the overall nozzle aerodynamic performance.

For the NACA0012 airfoil vane, the deflection angle of the flow increases with increase of the angle of attack. Increasing the angle of attack, however, causes the appearance of a sharp suction peak near the leading edge of the airfoil. At 10° angle of attack, supersonic flow appears, which may cause shock waves and potential flow separation, resulting in increased flow loss. The 2-Vane configuration does not provide enough flow turning without being set at high angles of attack. For the 4-vane configurations, the combination of azimuth angles of 50° and 120° is more effective for turning the flow than the 90° and 150° option, but causes more thrust loss.

The cambered airfoils yield larger flow deflections than the symmetric NACA0012 airfoil set at the same or smaller angle of attack but cause a large supersonic pocket with a strong shock in the rear part of the airfoil and thus are not good choices because of their large thrust and mass flow losses.

The deflection of the jet downward has the effect of reducing the turbulent kinetic energy on the lower part of the jet, which is correlated to the reduction of noise. On the other hand, regardless the choice of airfoils, higher flow turning is correlated to higher thrust and mass flow loss. Therefore, a balanced choice of the deflection angle must be made by looking at both these effects of the flow turning at the same time.

The classic airfoils studied in this paper were designed for flight in uniform external flows. They are found to be not suitable for use as internal deflector vanes in an accelerating flow. The symmetric NACA0012 airfoil has the tendency of overloading the front, causing a suction peak near the leading edge, while the cambered airfoils NACA7514 and NACA4412 tend to have a high load in the rear part of the airfoil, resulting in a large supersonic pocket and a strong shock wave. Future work should seek custom airfoils designed to work efficiently in an accelerating stream for effective flow turning and minimum penalties on the nozzle performance.

Acknowledgments

The support by NASA Cooperative Agreement NNX07AC62A (monitored by Dr. K.B.M.Q. Zaman) is gratefully acknowledged.

References

[1]Papamoschou, D., "New Method for jet Noise Reduction in Turbofan Engines," *AIAA Journal*, Vol. 42, No. 11, 2004, pp. 2245–2253.

[2]Papamoschou, D., "Fan Flow Deflection in Simulated Turbofan Exhaust," *AIAA Journal*, Vol. 44, No. 12, 2006, pp. 3088–3097.

[3]Papamoschou, D. and Nielsen, P., "Fan Flow Deflection for Supersonic Turbofan Engines," AIAA 2008-0039, Janurary 2008.

[4]Nielsen, P. and Papamoschou, D., "Optimization of Fan Flow Deflection for Supersonic Turbofan Engines," AIAA 2008-3061, May 2008.

[5]Papamoschou, D. and Liu, F., "Aerodynamics of Fan Flow Deflectors for Jet Noise Suppression," *Journal of Propulsion and Power*, Vol. 24, No. 3, 2008, pp. 437–445.

[6]Jameson, A., Schmift, W., and Turkel, E., "Numerical Solutions of the Euler Equations by Finite Volume Methods Using Runge-Kutta Time Stepping Schemes," AIAA 1981-1259, Janurary 1981.

[7]Bladwin, B. S. and Lomax, H., "Thin-Layer Approximation and Algebraic Model for Separation Flows," AIAA 1978-0257, Janurary 1978.

[8]Spalart, P. R. and Allmaras, S. R., "A One-Equation Turbulence Model for Aerodynamic Flows," AIAA 1992-0439, Janurary 1992.

[9]Wilcox, D., "Reassessment of the Scale Determining Equation for Advanced Turbulence Models," *AIAA Journal*, Vol. 26, No. 11, 1988, pp. 1299–1310.

[10]Menter, F., "Two-Equation Eddy-Viscosity Turbulence Models for Engineering Applications," *AIAA Journal*, Vol. 32, No. 8, 1994, pp. 1598–1605.

[11]Turkel, E., "A Review of Preconditioning Methods for Fluid Dynamics," *Applied Numerical Mathematics*, Vol. 12, No. 1, 1993, pp. 257–284.

[12]Liu, F. and Zheng, X., "A Strongly Coupled Time-Marching Method for Solving the Navier-Stokes and k-ω Turbulence Model Equations with Multigrid," *Journal of Computational Physics*, Vol. 128, No. 10, 1996, pp. 257–284.

[13]Xiong, J., Nielsen, P., Liu, F., and Papamoschou, D., "Computational Validation of Fan Flow Deflection for Supersonic Turbofan Engines," AIAA 2009-3254, Janurary 2009.

Table 1 Configurations for 2-vane and 4-vane cases

Configuration	Airfoil	C [mm]	x_{TE} [mm]	α_1 [deg]	ϕ_1 [deg]	α_2 [deg]	ϕ_2 [deg]
2V	NACA0012	3.0	-2	7.5	90	-	-
4V-A	NACA0012	3.0	-2	0.0	50	0.0	120
4V-B	NACA0012	3.0	-2	7.5	50	7.5	120
4V-C	NACA0012	3.0	-2	10.0	50	10.0	120
4V-D	NACA0012	3.0	-2	7.5	90	7.5	150
4V-E	NACA7514	3.0	-2	4.0	50	4.0	120
4V-F	NACA4412	3.0	-2	7.5	90	4.0	150

Table 2 Exhaust conditions

	Hot(cycle point)	Cold
$U_p[m/s]$	600	319
M_p	1.03	1.03
NPR_p	2.00	1.96
$U_s[m/s]$	400	213
M_s	1.15	0.65
NPR_s	2.25	1.33
A_s/A_p	1.4	1.40
U_s/U_p	0.67	0.67

Table 3 Aerodynamic performance of vane nozzle

Configuration	Mass loss	Thrust loss	Deflection angle
2V	0.046%	0.076%	0.584°
4V-A	0.008%	0.047%	0.00°
4V-B	0.152%	0.237%	0.938°
4V-C	0.266%	0.374%	1.242°
4V-D	0.073%	0.137%	0.814°
4V-E	0.56%	0.721%	1.331°
4V-F	0.182%	0.262%	1.168°

Table 4 Peak value of k^*

Configuration	${k^*}_{peak}, lower$	${k^*}_{peak}, upper$
Base	0.0212	0.0212
2V	0.0155	0.0235
4V-A	0.0216	0.0216
4V-B	0.0145	0.0254
4V-C	0.0126	0.0257
4V-D	0.0153	0.0264
4V-E	0.0119	0.0258
4V-F	0.0142	0.0268

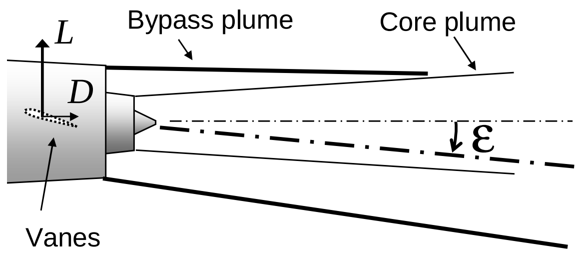

Figure 1. General concept of fan flow deflection.

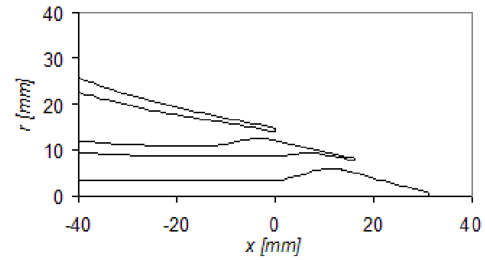

Figure 2. Coordinates of the bypass ratio BPR = 2.7 (B27) nozzle.

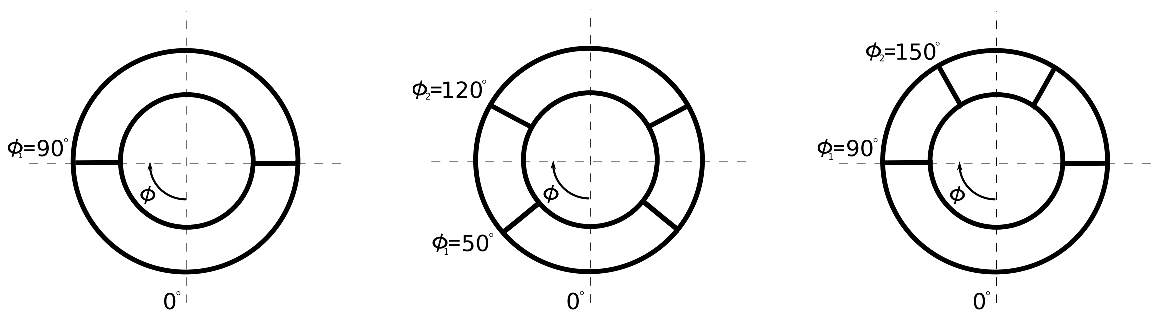

(a) 2V-configuration (b) 4V-A-C, 4V-E configurations (c) 4V-D, 4V-F configurations

Figure 3. Cross-section illustration of 2-vane and 4-vane configurations.

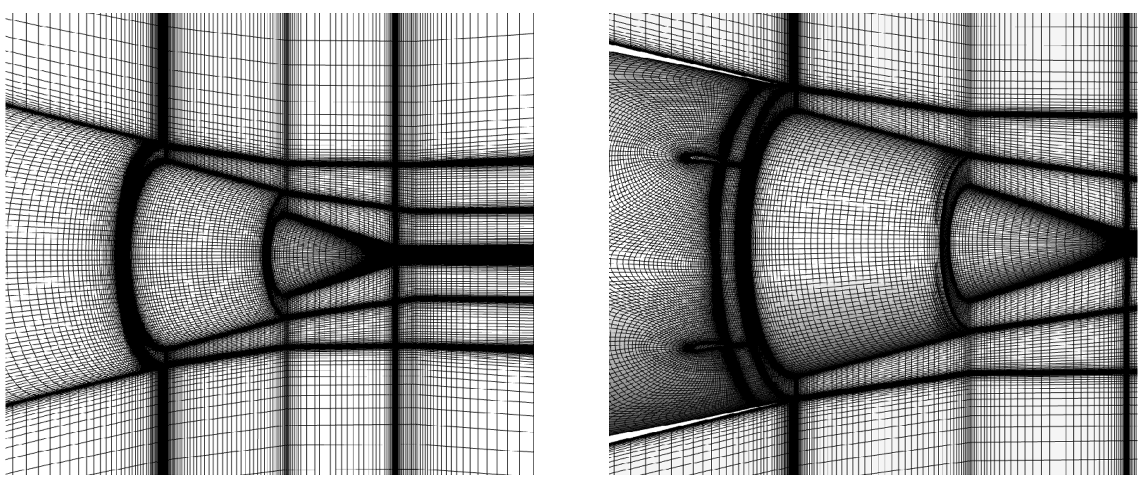

(a) (b)

Figure 4. Computational grid of vane nozzle.

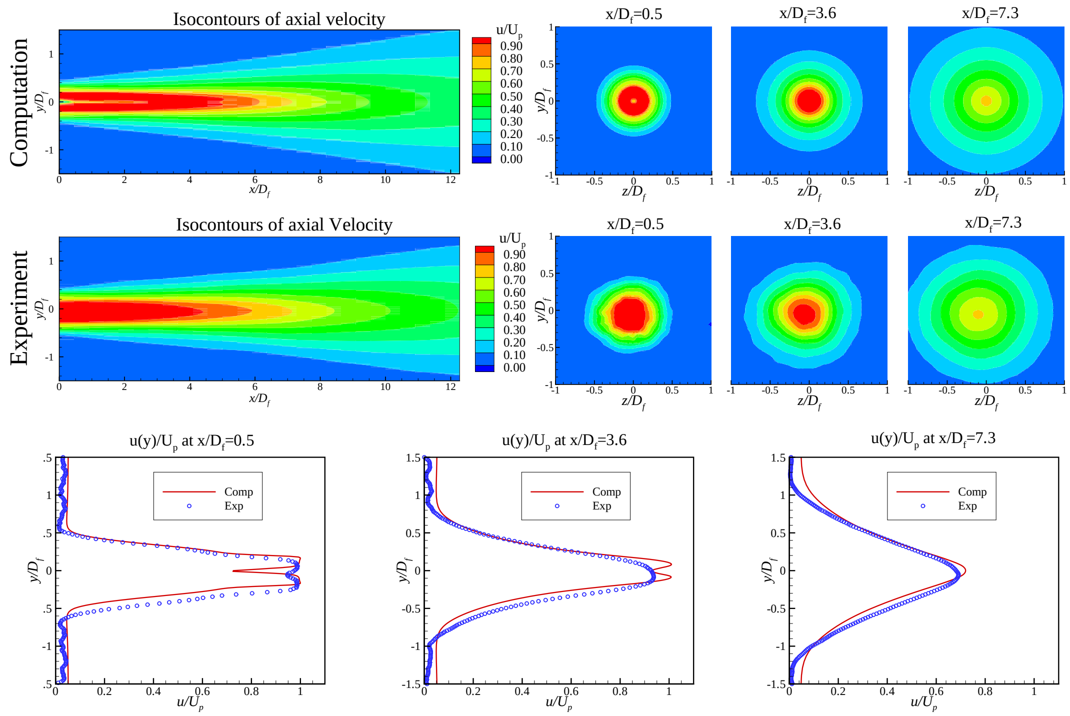

(a) Baseline nozzle

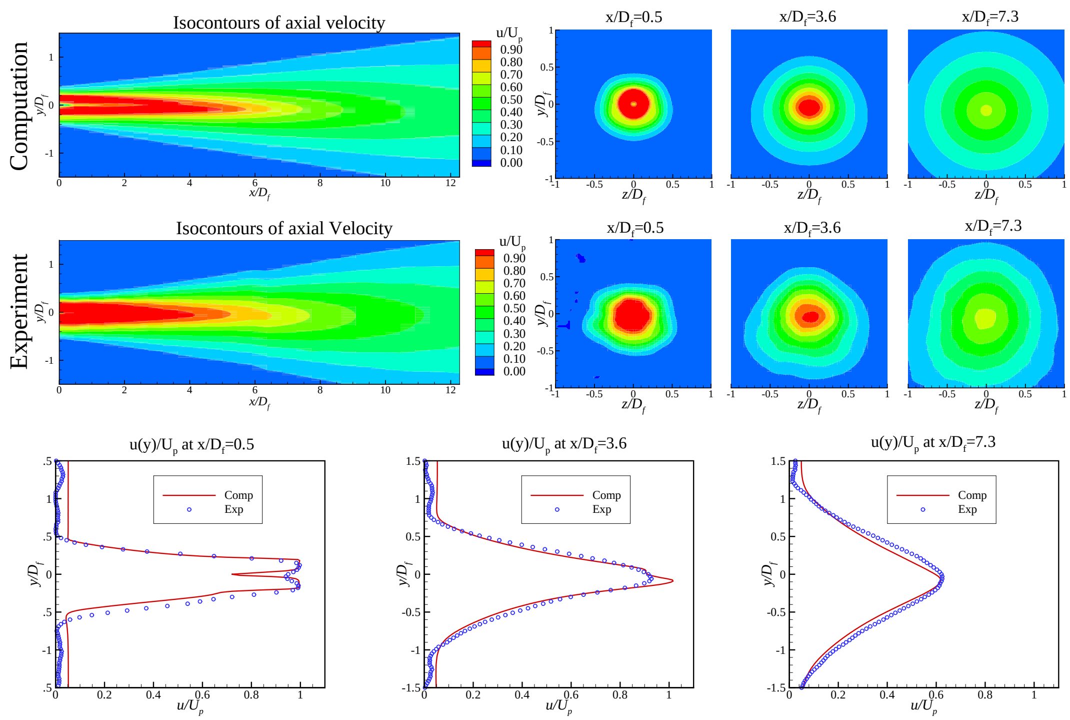

(b) 4V-D nozzle

Figure 5. Comparison of computational and experimental velocity field (cold condition).

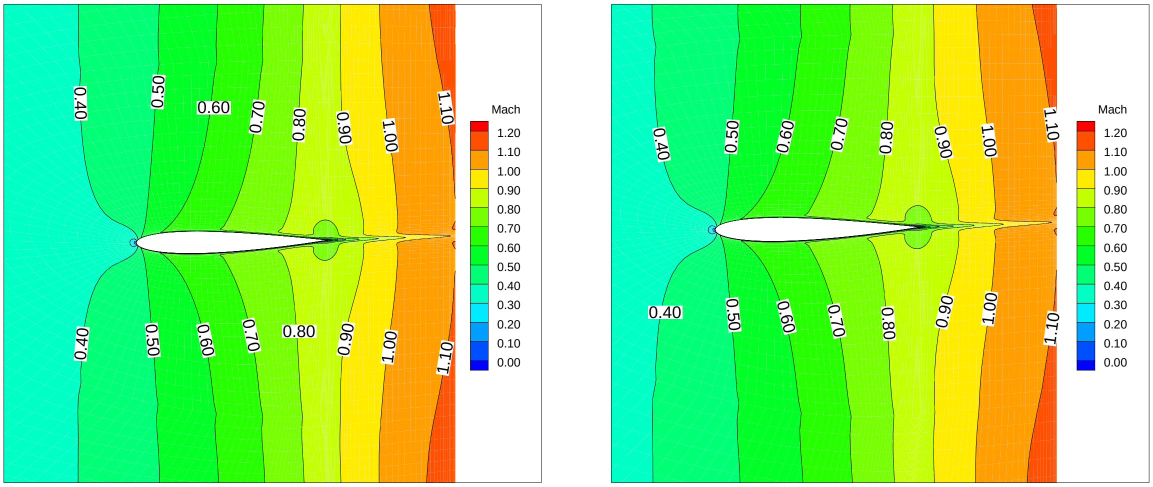

(a) $\phi_1 = 50°$, $\alpha_1 = 0°$ (b) $\phi_2 = 120°$, $\alpha_2 = 0°$

Figure 6. Mach number contours on midplane of vane for the 4V-A nozzle, NACA0012 airfoil.

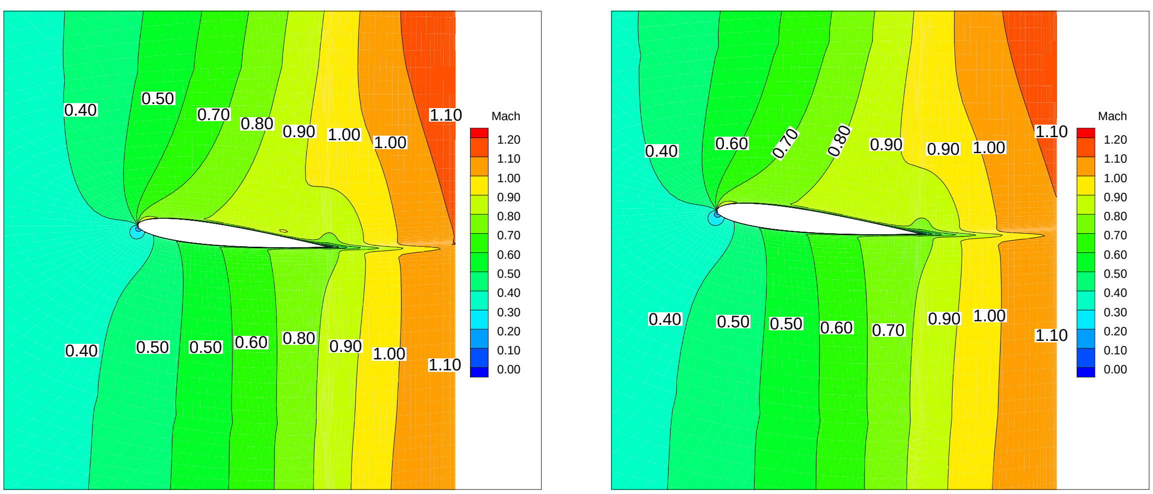

(a) $\phi_1 = 50°$, $\alpha_1 = 7.5°$ (b) $\phi_2 = 120°$, $\alpha_2 = 7.5°$

Figure 7. Mach number contours on midplane of vane for the 4V-B nozzle, NACA0012 airfoil.

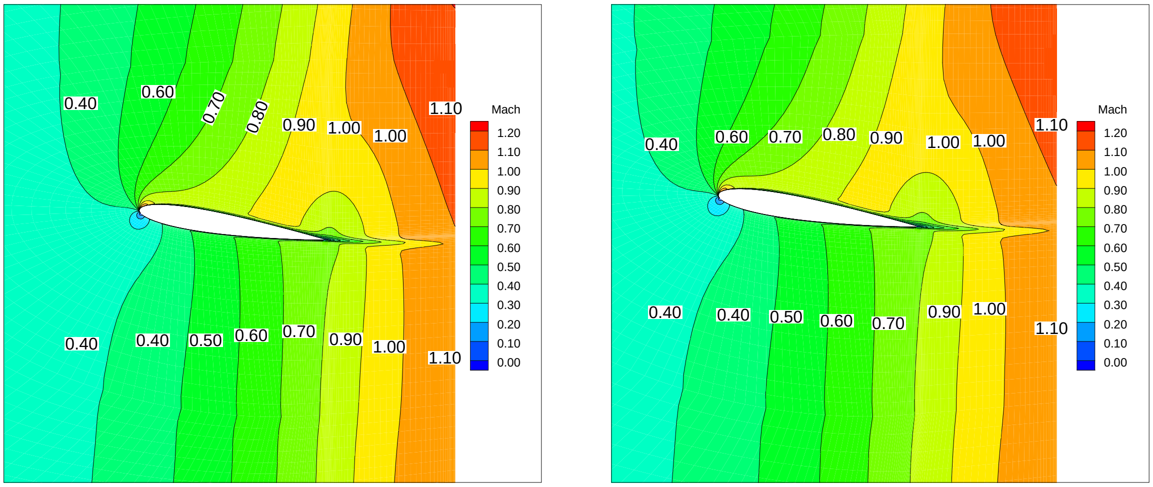

(a) $\phi_1 = 50°$, $\alpha_1 = 10°$ (b) $\phi_2 = 120°$, $\alpha_2 = 10°$

Figure 8. Mach number contours on midplane of vane for the 4V-C nozzle, NACA0012 airfoil.

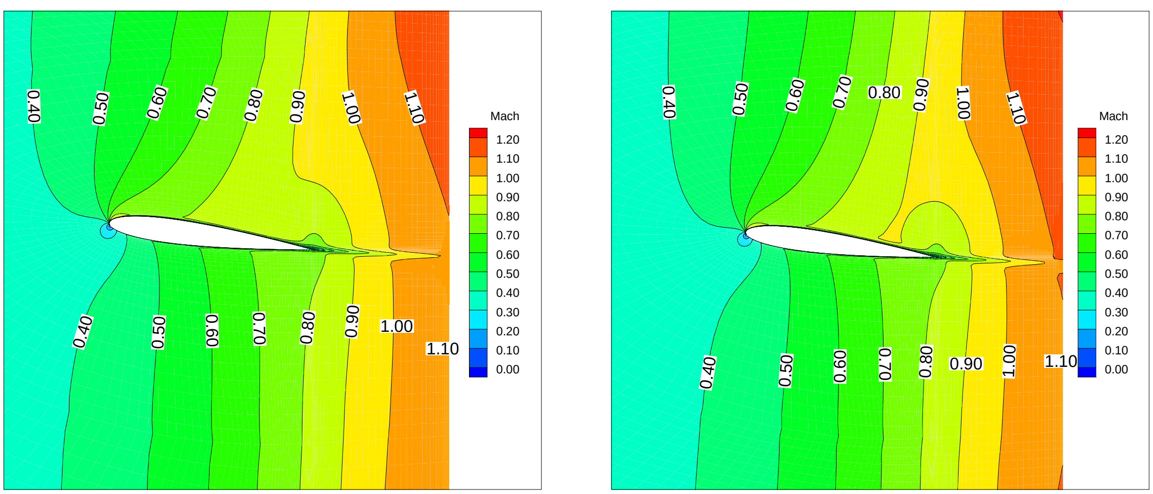

(a) $\phi_1 = 90°$, $\alpha_1 = 7.5°$ (b) $\phi_2 = 150°$, $\alpha_2 = 7.5°$

Figure 9. Mach number contours on midplane of vane for the 4V-D nozzle, NACA0012 airfoil.

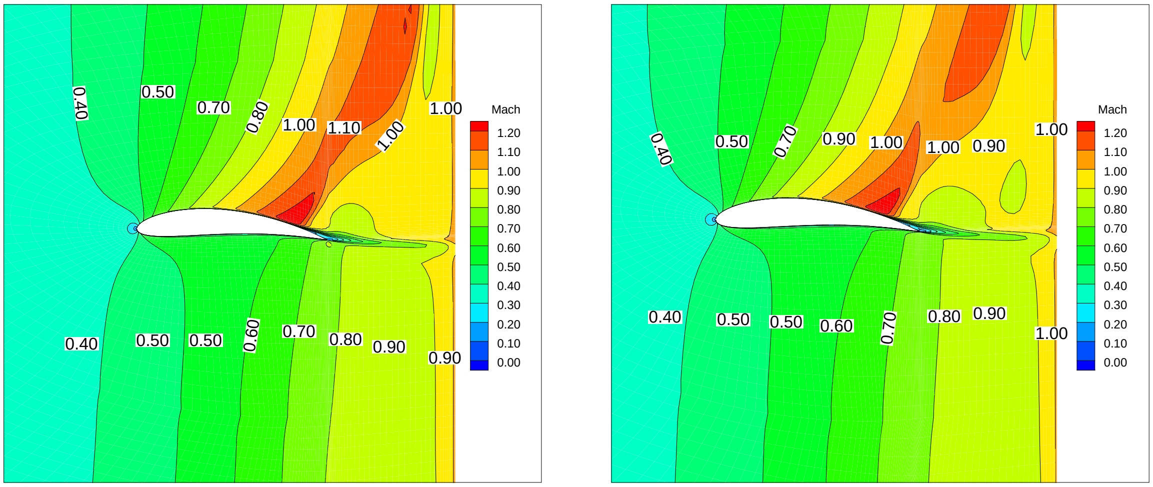

(a) ϕ_1= 50°, α_1= 4°

(b) ϕ_2= 120°, α_2= 4°

Figure 10. Mach number contours on midplane of vane for the 4V-E nozzle, NACA7514 airfoil.

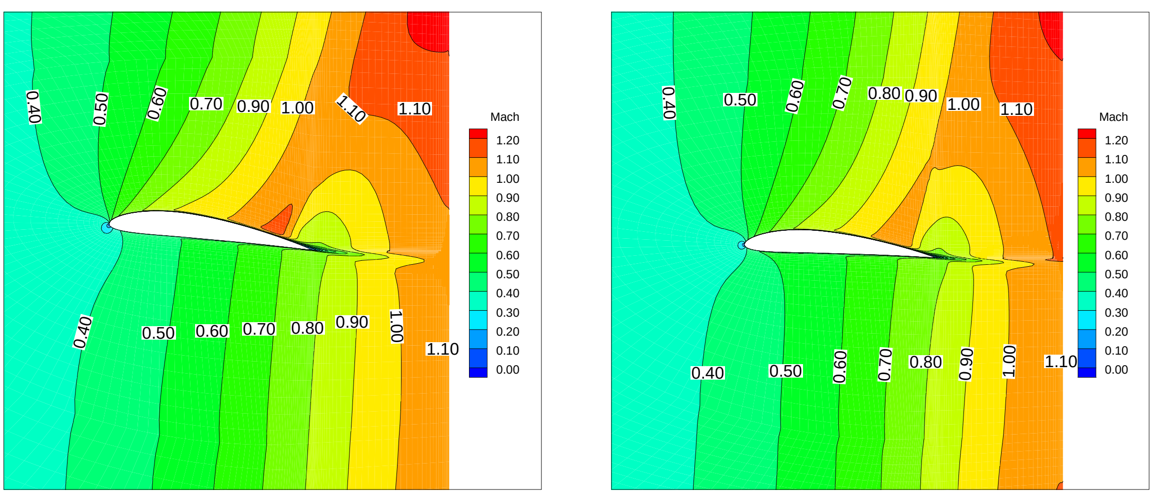

(a) ϕ_1= 90°, α_1= 7.5°

(b) ϕ_2= 150°, α_2= 4°

Figure 11. Mach number contours on midplane of vane for the 4V-F nozzle, NACA4412 airfoil.

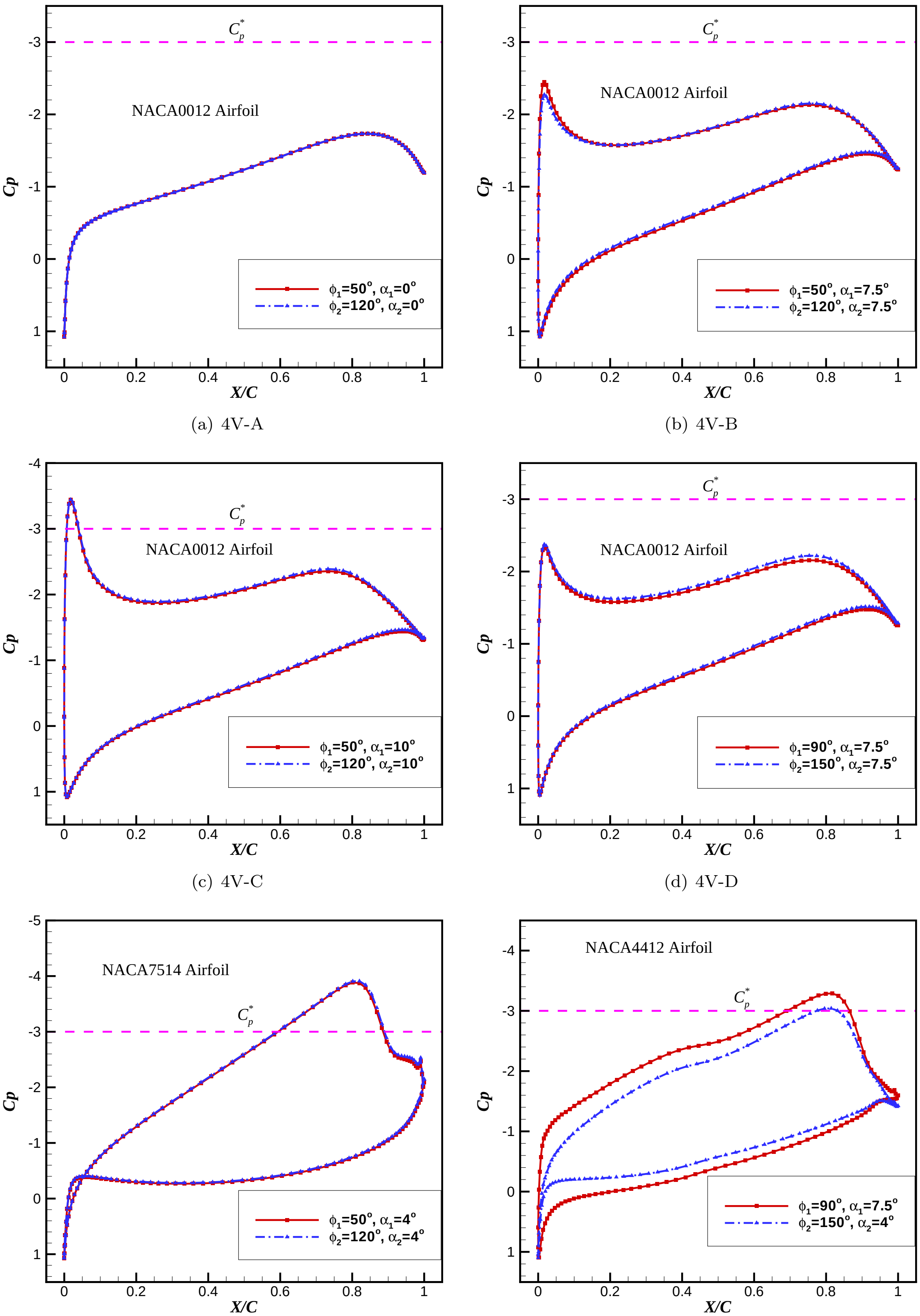

(a) 4V-A (b) 4V-B

(c) 4V-C (d) 4V-D

(e) 4V-E (f) 4V-F

Figure 12. Pressure coefficient on midplane of vane for the 4-V configurations.

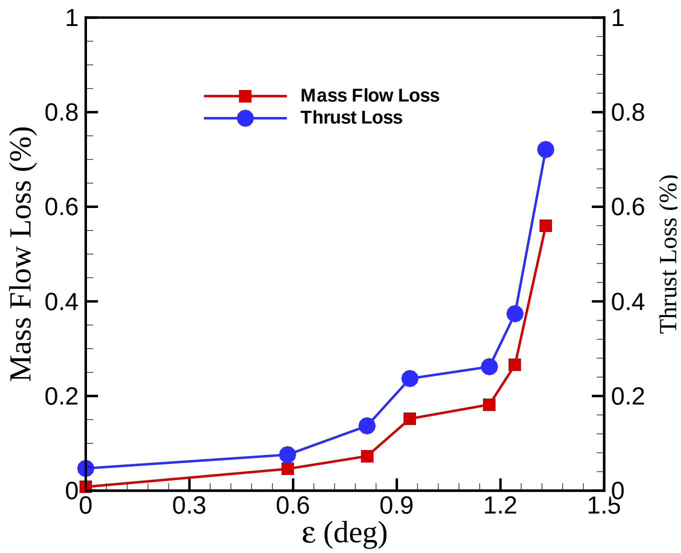

Figure 13. Mass flux loss and thrust loss versus plume deflection angle.

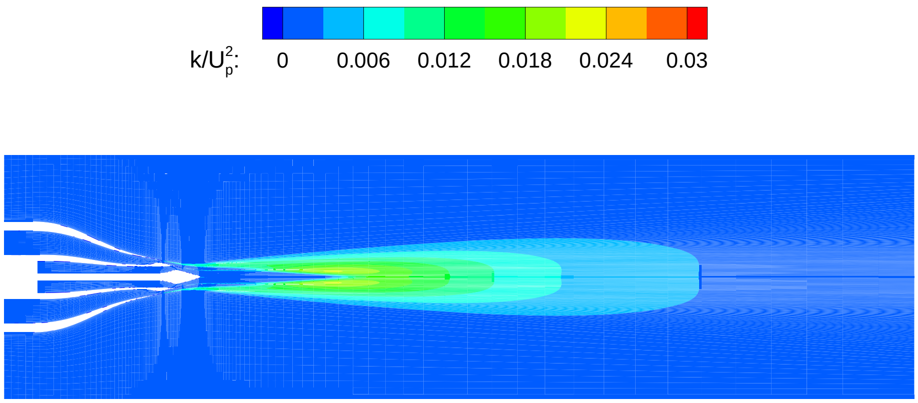

(a) Baseline nozzle

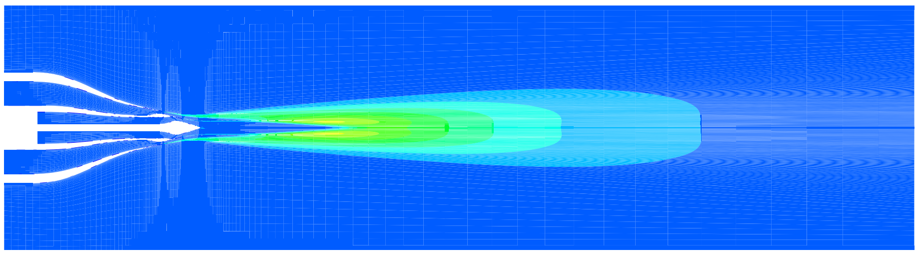

(b) 4V-A nozzle

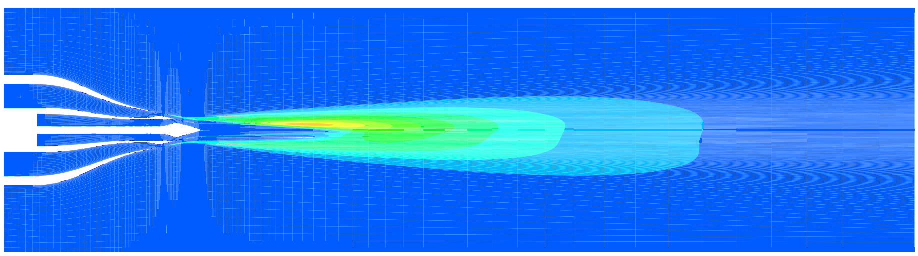

(c) 4V-B nozzle

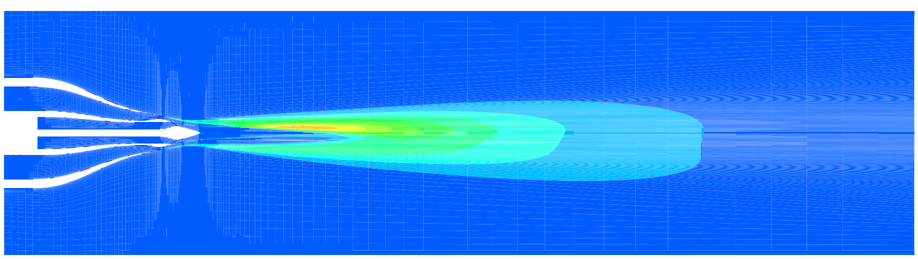

(d) 4V-C nozzle

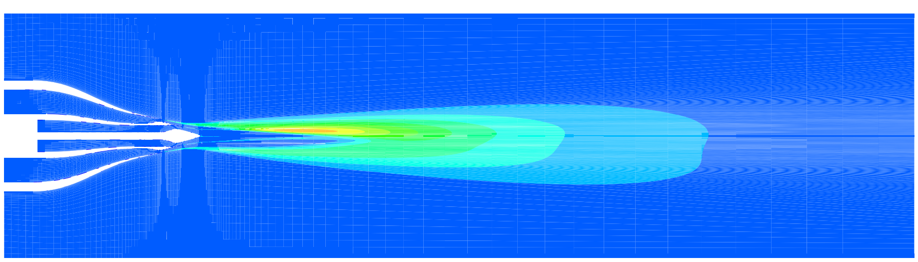

(e) 4V-E nozzle

Figure 14. Contours of turbulent kinetic energy on symmetry plane.

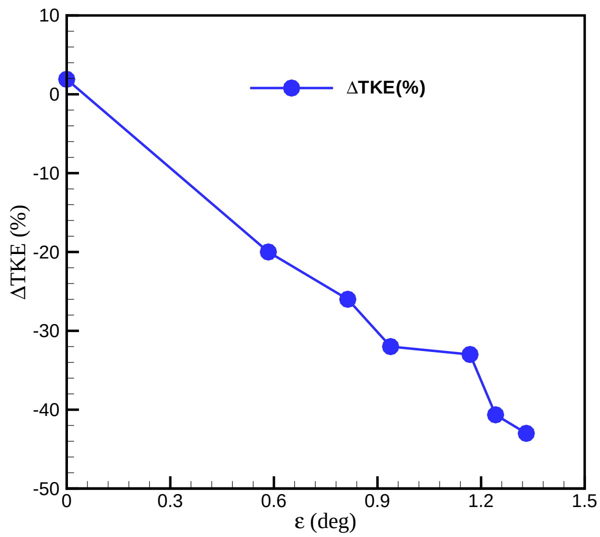

Figure 15. Percent turbulent kinetic energy reduction on lower side of jet versus plume deflection angle.

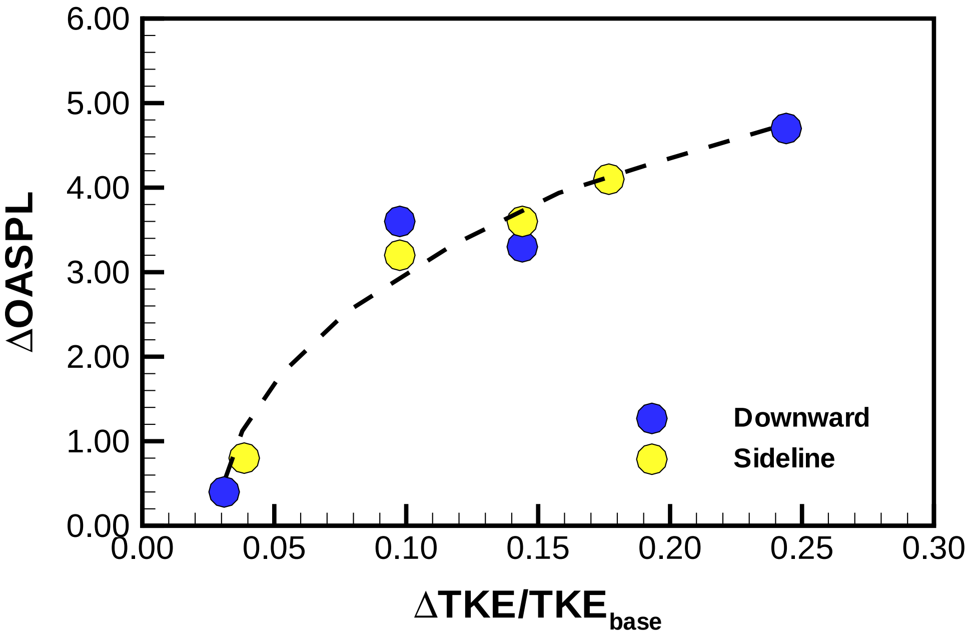

Figure 16. Correlation between reduction in peak overall sound pressure level (OASPL) and normalized maximum turbulent kinetic energy (TKE).